SCIENTIFIC REPORTS

OPEN

Role of cobalt cations in short range antiferromagnetic Co_3O_4 nanoparticles: a thermal treatment approach to affecting phonon and magnetic properties

Received: 1 August 2017
Accepted: 14 December 2017
Published online: 10 January 2018

Swati R. Gawali[1], Ashish Chhaganlal Gandhi[2], Shrikrushna Shivaji Gaikwad[2], Jayashree Pant[3], Ting-Shan Chan[4], Chia-Liang Cheng[2], Yuan-Ron Ma[2] & Sheng Yun Wu[2]

We report the phonon and magnetic properties of various well-stabilized Co_3O_4 nanoparticles. The net valence in cobalt (II)/(III) cation can be obtained by subtracting the Co^{2+} ions in tetrahedral interstices and Co^{3+} ions in the octahedral interstices, respectively, which will possess spatial inhomogeneity of its magnetic moment via Co^{2+} in tetrahedra and Co^{3+} in octahedral configurations in the normal spinel structure. Furthermore, the distribution of Co^{2+}/Co^{3+} governed by various external (magnetic field and temperature) and internal (particle size and slightly distorted CoO_6 octahedra) sources, have led to phenomena such as a large redshift of phonon-phonon interaction and short-range magnetic correlation in the inverse spinel structure. The outcome of our study is important in terms of the future development of magnetic semiconductor spintronic devices of Co_3O_4.

Nanomaterials usually exhibit a number of unique and enhanced properties, which may strongly differ from those observed in their bulk counterpart. In the last decade, research on the effects of the finite size on the structural, optical and magnetic properties of Co_3O_4 have attracted enormous attention because of its wide range of important potential applications as a gas sensor[1], data storage[2], magnetic semiconductors[3], electrochemical devices[4], heterogeneous catalysts[5], anode materials in Li-ion rechargeable batteries[6], solid-state sensors[3], solar energy absorbers, pigments[7–9] etc. The functioning of all these devices is strongly influenced by the different sample synthesis methods[3], point defects (such as cation or anion vacancies)[10], their morphology (such as nanobelts, nanorods, nanospheres, nanocubes, nanowires and nanoflowers) and nanosized effect[11,12]. Recently, Casas-Cabanas *et al.*[7] carried out a crystal structural investigation of Co_3O_4 nanoparticles (NPs) with size varrying from 32 nm to a few micrometers. In their comprehensive analysis, they discovered that small size particles having high cobalt vacancies exhibit a strong variation in the intensity ratio of (111)/(220) XRD diffraction peaks. Similar high intense (111) diffraction peak from Co_3O_4 have also been reported by Furlanetto[13] and Cao *et al.*[14]. Co_3O_4 has a simple spinel structure ($Fd\bar{3}m$) having oxygen ions (32e Wyckoff sites) slightly displaced from the ideal (1/4, 1/4, 1/4) position with cations Co^{2+}(8a Wyckoff sites) and Co^{3+}(16d Wyckoff sites) distributed among tetrahedral and octahedral sites, respectively. It also exhibits *p*-type semiconducting properties[15] because of cationic (cobalt) vacancies resulting in an oxygen rich spinel. However, unlike mono-oxides, the choice of the cationic vacancy location in a spinel structure is much more complex as it could be either on Co^{2+} sites, Co^{3+} sites, or both. Angelov *et al.*[16] deduced from electron paramagnetic resonance (EPR) analysis that cobalt vacancies in oxygen-rich $Co_{3-x}O_4$ powder resides on octahedral sites. Furthermore, most of the above applications of Co_3O_4 are based on the use of nanomaterials with magnetic properties that often differ considerably from those of their bulk counterpart. Bulk Co_3O_4 is an antiferromagnetic (AFM)[17], having a Néel temperature T_N between 30 K[18,19]

[1]Department of Physics, CES's Dr. A. B. Telang Sr. College, Savitribai Phule Pune University, Pune, 411007, India. [2]Department of Physics, National Dong Hwa University, Hualien, 97401, Taiwan. [3]Department of Physics, Abasaheb Garware College, Savitribai Phule Pune University, Pune, 411007, India. [4]National Synchrotron Radiation Research Center, Hsinchu, 30076, Taiwan. Correspondence and requests for materials should be addressed to S.Y.W. (email: sywu@mail.ndhu.edu.tw)

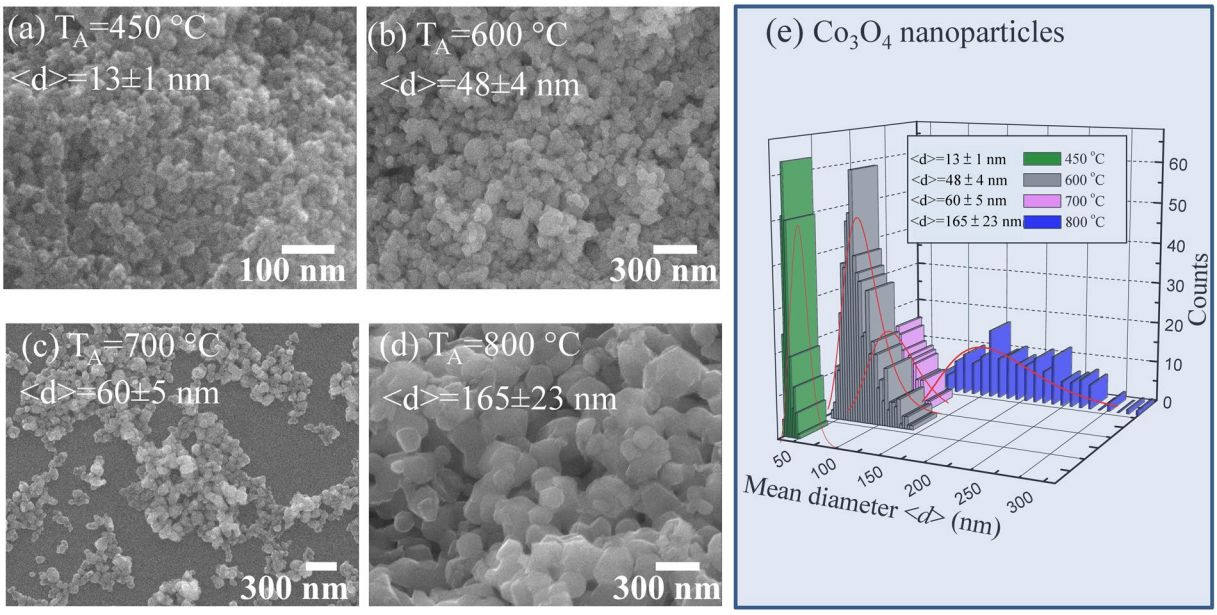

Figure 1. (**a**)–(**d**) A portion of SEM images of 450 °C to 800 °C annealed samples representing size distribution and morphology. (**e**) Histogram of diameter distribution of Co_3O_4 NPs of various samples calculated from the SEM images, where the solid-line represents log-normal distribution function fit.

and 40 K[17]. Resnick *et al.*[20] reported superparamagnetic (SPM) temperature $T_B \sim 5.4$ K and reduced $T_N = 15 \pm 2$ K from 4.34 nm Co_3O_4 nanoparticles. The observed SPM behavior and reduced T_N was ascribed to uncompensated spins, which are attributed to structural inhomogeneities, defects, and finite size effects.

Here, it is important to note that magnetic moments in Co_3O_4 arise solely because of spins of Co^{2+} ions having a small contribution from spin-orbit coupling[17]. On the other hand, the Co^{3+} ions at the octahedral sites are diamagnetic as a consequence of the splitting of 3d levels by the octahedral crystal field and complete filling of t_{2g} levels due to which vacancies at octahedral sites do not contribute to net magnetization. Therefore, apart from XRD and Raman measurements, a rigorous magnetic study of Co_3O_4 nanoparticles having cobalt vacancies can help us in locating their sites in the spinel structure. In this study, details of the synthesis, as well as the structural and magnetic properties of various sizes of Co_3O_4 nanoparticles are presented. This work aims to investigate the influence of cobalt cations and the finite size effect on the induction of short-range magnetic correlation and Néel temperature.

Results

Morphological and stoichiometric analysis. The well dispersed and pseudo-spherical nanoparticles of Co_3O_4 are visible from a portion of SEM images after annealing at 450, 600, and 700 °C, as shown in Fig. 1(a)–(c). The interconnecting nanoparticles were stuck together in clusters because of electrostatic effects as well as an artifact of the drying of the aqueous suspension, revealing a nanoparticle agglomeration behavior. The clustering makes an evaluation of the size distribution possible. A similar behavior of nanoparticle agglomeration has also been reported from NiO[21], ZnO[22] nanoparticles, and NiO nanowalls[23]. However, the samples annealed at 800 °C (Fig. 1(d)) formed sinter necks between them, showing a sintering behavior. To estimate the mean size of nanoparticles, the distribution of particle diameter can be calculated from the SEM images and described by using log-normal distribution function, as shown in Fig. 1(e). The log-normal distribution function is defined as follows: $f(d) = \frac{1}{\sqrt{2\pi}\,d\sigma}\, exp\left[-\frac{(lnd - ln <d>)^2}{2\sigma^2}\right]$, where $<d>$ is the mean diameter and σ is the standard deviation of the function. The mean diameter and standard deviation of Co_3O_4 nanoparticles annealed at 450, 600, 700, and 800 °C were obtained after fitting the log-normal function, that is $<d> = 13 \pm 1, 48 \pm 4, 60 \pm 5, 165 \pm 21$ nm and $\sigma = 0.23 \pm 0.11, 0.30 \pm 0.09, 0.27 \pm 0.09, 0.41 \pm 0.16$ nm, respectively. The value of σ is below 0.3 nm for nanoparticles annealed at 450, 600, and 700 °C indicating the distributions of nanoparticles is confined within a narrow range[24], whereas the distribution of nanoparticles annealed at 800 °C is confined within the intermediate range[25]. Energy-dispersive spectroscopy (EDS) technique is used to detect the chemical purity and estimate the atomic percentage in a given sample[23,24]. The EDS spectra of various annealing temperatures plotted in Fig. 2(a) are associated with a series of elemental cobalt and oxygen, that can be assigned to Co-Lβ_1, Co-Kα_1, Co-Kβ_1, and O-Kα_1. The small, intense peaks of C-Kα_1 and Si-Kα are originated from the contribution of carbon film on the Cu-grid and the silicon substrate as a consequence of mounting the sample[21].The estimated atomic percentage ratio of Co/O obtained from EDS spectra reveals an increasing behaviour with the annealing temperature and approaches to a value of 0.692 after annealing at 800 °C. The value is close to the theoretical stoichiometric value of 0.75[10] for Co_3O_4 as shown in Fig. 2(b). Significantly, a small Co/O atomic percentage ratio of 0.45 obtained in the sample annealed at 450 °C, has attracted more interest, indicating a huge deficiency of Co in the sample and ~0.6 times that of the bulk value. The effect of annealing in an ambient atmosphere resulted in an increase of the

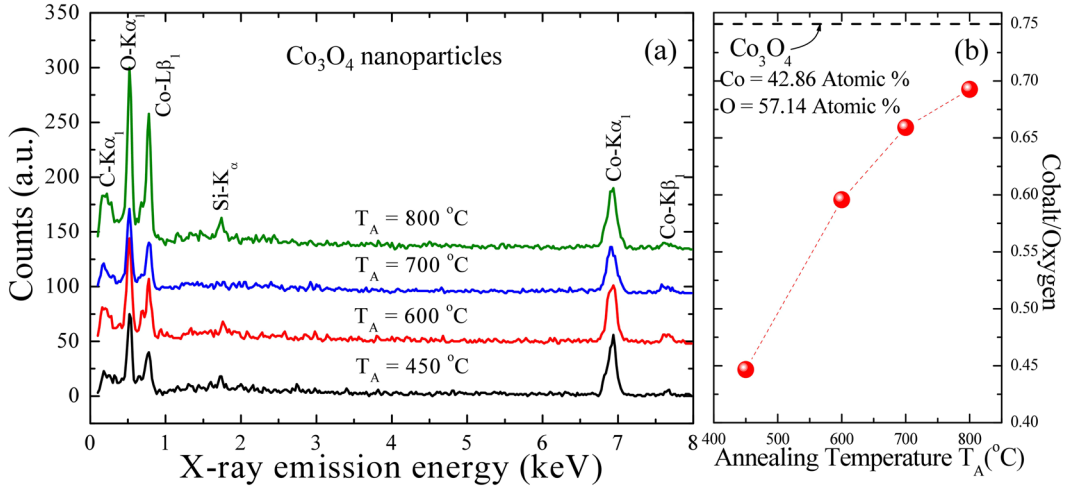

Figure 2. (**a**) Plot of EDS spectra for Co_3O_4 NPs, which are shifted vertically for clear visibility. (**b**) The variation in the ratio of cobalt/oxygen with respect to the crystalline size of NPs.

Co/O ratio, which approached to the value of bulk stoichiometry after annealing at 800 °C. George *et al.*[10] also reported a similar effect of annealing on the stoichiometry of nano-crystalline Co_3O_4 ultra-fine fibers synthesized by sol-gel electrospinning. In their analysis, they observed the effect of the annealing result in an increase of the crystallinity, grain size ($<d> = 25.3$ nm at 400 °C and $<d> = 42.9$ nm at 500 °C) of Co_3O_4 nano-fibers. However, there are also reports in which either a slightly increased[26] or almost similar[11,27] value of Co/O atomic percentage ratio as that of the theoretical value has been reported for various sized Co_3O_4 nanoparticles synthesized by different chemical and physical techniques. This synthesis method plays an important role in defining the stoichiometry and crystallinity of nanomaterials. In this set of samples, the observed cobalt vacancies could be either at octahedral (Co^{3+}), tetrahedral (Co^{2+}) sites or at both the sites of Co_3O_4, which will be discussed later in the text.

X-ray diffraction and analysis. The detailed crystalline structure and strain in various sized Co_3O_4 nanoparticles can be investigated by using a high-energy synchrotron x-ray diffraction technique. For the purpose of structural analysis, the Rietveld refinement of x-ray patterns of different Co_3O_4 samples was carried out by using a GSAS software package. Figure 3 (a)–(d) display the x-ray diffraction patterns taken at various annealing temperatures, where the red, green, and blue curves indicate the fitted pattern, the background, and the difference between the observed and fitted pattern, respectively. As we know, Co_3O_4 adopts the normal spinel structure shown in Fig. 3(e) with Co^{2+} ions in tetrahedral interstices and Co^{3+} ions in the octahedral interstices of the cubic close-packed lattice of oxide anions, as plotted into Fig. 3(f). The obtained refined lattice parameters indicate that the nanoparticles are crystallized as a cubic spinel cobalt oxide (Co_3O_4) with a space group of $Fd\bar{3}m$ (No. 227) without any trace of additional impurity. The fitted parameters are summarized in the supplementary information of Table S1. Significant broader diffraction peaks are clearly visible through naked eyes from the x-ray pattern of the sample annealed at 450 °C, in agreement with the nanometric nature of the sample as can be seen in Figure 3(a)[7]. With an increase of annealing temperature, diffraction peaks and the full width at half-maximum (*fwhm*) become sharper and broaden, as a result of an increase in crystalline size and the loss of internal microstrains[7]. The observed broadening of the diffraction peak reveals a short-range crystalline behavior that can be fitted by the Gaussian function[28]. The value of *fwhm* of the most intense diffraction peak [311] tabulated in the supplementary information of Table S1 showed a rapid increase from 0.078 ± 0.003 to 0.308 ± 0.002 as the grain size decreased from the 85 ± 6 nm to 15 ± 1 nm, signaling the finite size effect or the combined effect of size and strain. The grain size d_{XRD} and the strain (η) of various sized Co_3O_4 nanoparticles were estimated by using Williamson-Hall (W-H) plot[29] and the well-known Scherrer formula[30] $\beta = \beta_{size} + \beta_{strain} = \frac{1}{cos\theta}\left(\frac{k\lambda}{< d_{XRD} >} + 4\eta sin\theta\right)$, where β is the *fwhm* of the diffraction peak, k is the Scherrer constant ($= 0.94$) for spherical nanoparticles, θ is the diffraction angle, λ is the incident x-ray wavelength, and η is the strain parameter, respectively. Figure 4(a) shows the plot of $\beta\cos\theta/k\lambda$ versus $4\sin\theta/k\lambda$ for all Co_3O_4 samples. The intercept of the linear fit to the data point in the W-H plot gives the value of grain size d_{XRD}, whereas the slope presents the value of strain. The estimated value of strain is below 0.0011, indicating that nanoparticles are free from any strain and therefore the broadening of diffraction peaks is exclusively because of the finite size effect. The value of strain is close to the estimated value of 0.00095 from the W-H plot reported from 15 nm size Co_3O_4 nanoparticles synthesis by using a microwave technique[12]. Rao *et al.*[31] reported a value of $\eta = 0.0070$ from ~13 nm size Co_3O_4 nanoparticles synthesized by a urea-based combustion method which is ~7 times higher than the observed value. The observed grain size after extrapolating the linear fit in the W-H plot of Co_3O_4 nanoparticles annealed at 450, 600, 700, and 800 °C were 15 ± 1, 54 ± 4, 62 ± 3, and 85 ± 6 nm, respectively. The observed grain size of 15 ± 1, 54 ± 4, and 62 ± 3 nm (from W-H plot) and mean nanoparticle diameter of 13 ± 1, 48 ± 4, and 60 ± 5 nm (from the portion of SEM images) of various annealed Co_3O_4 nanoparticles at $T_A = 450$, 600 and 700 °C, respectively, are in excellent agreement with each other, revealing the formation of

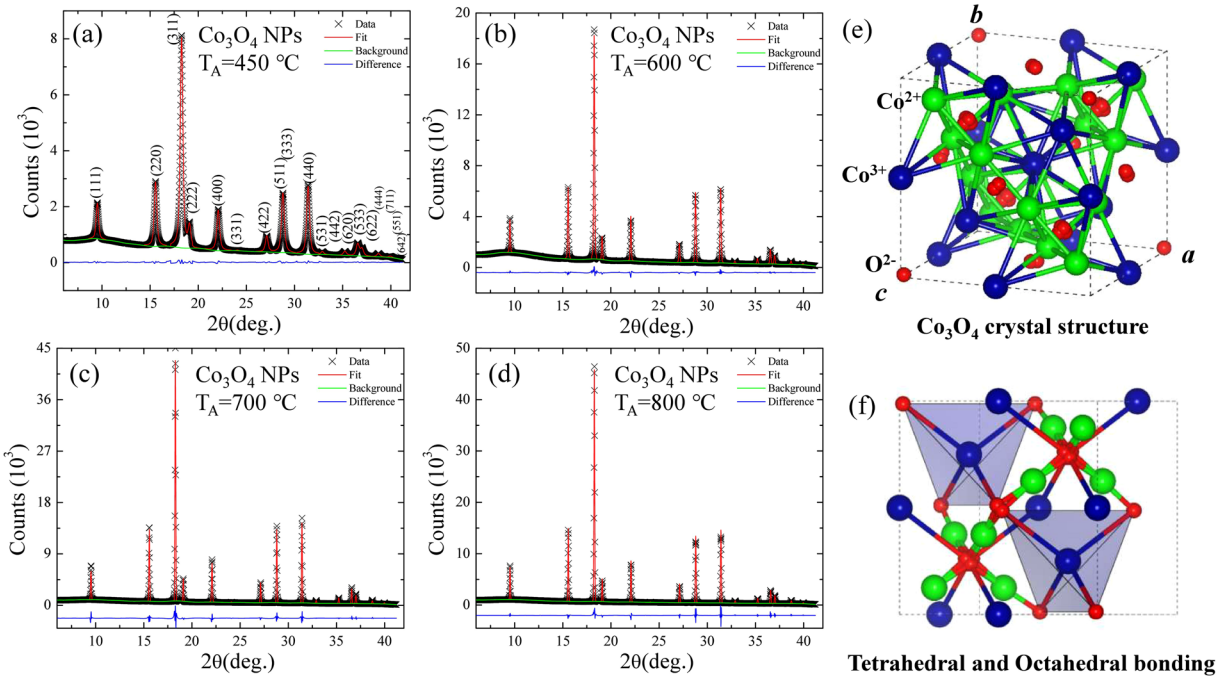

Figure 3. (**a**)–(**d**) Observed x-ray patterns (black crosses) of Co_3O_4 NPs synthesized at various annealing temperatures $T_A = 450$, 600, 700, and 800 °C, respectively. The solid red lines are the Rietveld refinement fit to x-ray patterns. The difference (blue curve) between the observed and the fitted patterns is plotted at the bottom of figure. (**e**) Crystal structure of Co_3O_4 NPs. (**f**) Plot of Co^{2+} ions in tetrahedral interstices and Co^{3+} ions in the octahedral interstices of the cubic close-packed lattice of oxide anions.

nanoparticles with a single domain. However, the grain size of Co_3O_4 nanoparticles annealed at $T_A = 800$ °C, 85 ± 6 nm obtained from x-ray diffraction differs significantly from the result of SEM ($<d> = 165 \pm 23$ nm). The discrepancy of obtained particle size is due to the agglomeration behavior of nanoparticles at higher annealing temperatures, which resulted in the formation of multiple domains within each nanoparticle[21–23]. The corresponding particle size d_{XRD} of the Co_3O_4 nanoparticles versus the annealing temperatures are shown in Fig. 4(b). As seen in Fig. 4(b), the estimated values of d_{XRD} versus the annealing temperature T_A are plotted, revealing an increase with the increase in the particle size. The *red solid curve* indicates the fit of the data to the theoretical curve for an exponential function, $\langle d_{XRD} \rangle = d_o + \beta \exp(-T_A/T_{AO})$, where $d_o = 122(5)$ nm, $\beta = -337(11)$ nm, and $T_{AO} = 392(29)$ °C represents the initial constant and the fitted parameters, respectively. A slight lattice expansion of 0.15% (percent deviation) was observed from the $T_A = 450$ °C sample and as the annealing temperature T_A increased further, it approaches to the bulk value of ~8.09 Å[19] as shown in Fig. 4(c). A similar lattice expansion has been reported previously from Co_3O_4 nanoparticles synthesized by chemical means[7,32]. Moreover, many metal oxides show lattice expansion with a reduction of particle size which could be either because of the finite size effect, cation/anion vacancies, lattice stress *etc*. However, in general, Co_3O_4 nanoparticles synthesized by using different methods exhibit the common trend of lattice expansion with an increase of particle size[33–35]. For charge neutrality, some of the Co^{3+} vacancies could be substituted by Co^{2+} ions, which resulted in the contraction of the Co^{2+}–O^{2-} bond length. Therefore, further investigations of net valences are expected in the next step. This can be calculated quantitatively using the bond valence method developed by Brown and O'Keefe[36]. The general principles of the bond valence method can be summarized as $v_{jk} = exp\left[\left(R_{jk} - d_{jk}\right)/b\right]$, where v_{jk} is the bond valence associated with a bond of length d_{jk} between the neighboring atoms j and k, the bond valence parameter R_{jk} is the distance corresponding to a bond valence $v = 1.0$ v.u. and V_j is the sum valence of $\sum_k v_{jk}$. The universal constant b is equal to 0.37 Å. The net valence in the Co^{2+}-O^{2-} bond and the Co^{3+}-O^{2-} bond can be obtained by subtracting the Co^{2+} ions in tetrahedral interstices and the Co^{3+} ions in the octahedral interstices, respectively. The net valences of Co^{2+} and Co^{3+} at various annealing temperatures are summarized in the supplementary information of Table S2. One of the important differences in our study from earlier reported crystal structures (bulk Co_3O_4[19]) lies in the typical bond distances of Co^{2+}-O^{2-} and Co^{3+}-O^{2-}. The Co^{2+}-O^{2-} bond lengths (obtained from the Rietveld refined structure) vary from 1.917 Å to 1.91 Å in the present study as compared with 1.929 Å as reported earlier[19]. In additione typical bond distance of Co^{3+}-O^{2-} in our case ranges from 1.935 to 1.938 Å as compared to that reported earlier value of 1.916 Å in slightly distorted CoO_6 octahedra. It may also be possible that some of the Co sites will have Co^{3+} instead of Co^{2+} which would further give rise to the decreasing of net valence $Co^{3+}(0)$ and the increasing of net valence $Co^{2+}(0)$ with increasing annealing temperature, as can be seen in Fig. 5. This might result in the shortening of the Co^{2+}-O^{2-} bond lengths accompanied by an increase in Co^{3+}-O^{2-} bond lengths at least for that oxygen which is connected to both Co^{2+} and Co^{3+}, which will possess spatial inhomogeneity of its magnetic moment via Co^{2+} in tetrahedra and Co^{3+} in octahedral configurations in the normal spinel structure. However, the distribution of Co^{2+}/

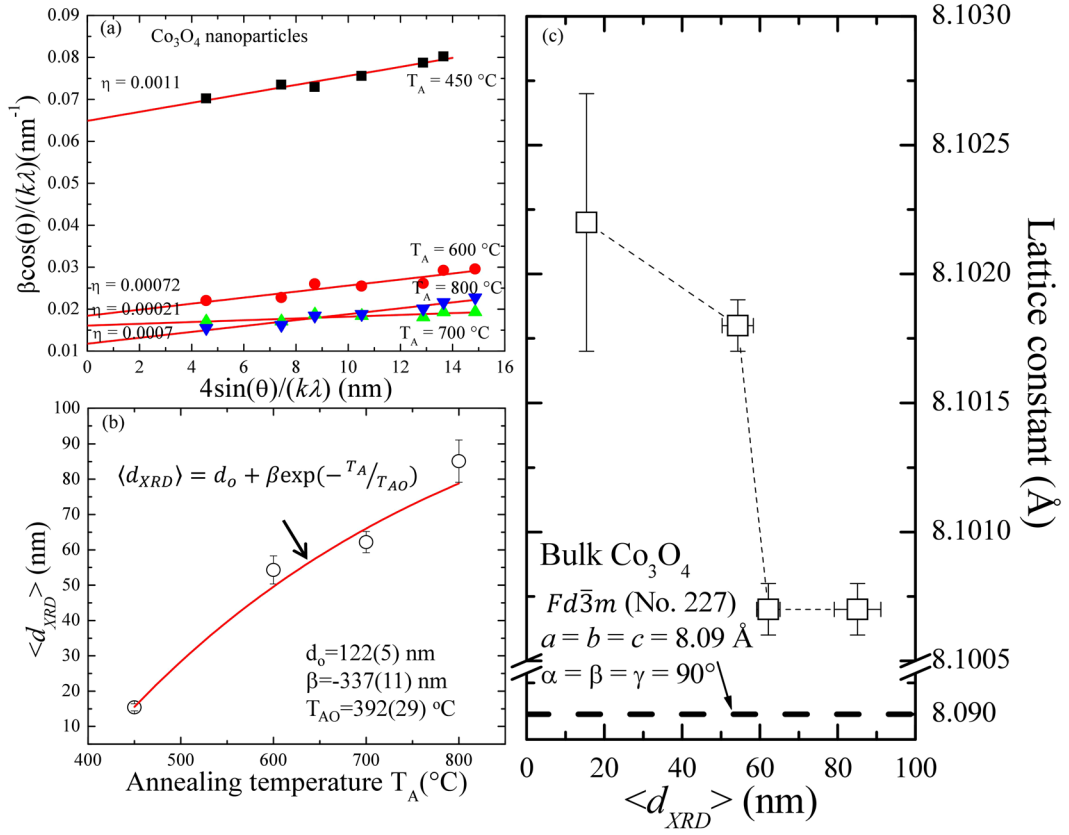

Figure 4. (**a**) Linear fit obtained using the Williamson−Hall correlation for each Co_3O_4 NPs, where the slope of the graph gives the mean strain and the intercept of the line with the y axis gives the inverse particle size. (**b**) Annealing temperature T_A dependence of the mean nanoparticle diameter $<d_{XRD}>$, where the solid line shows the fit to the exponential function and the fitted values are indicated. (**c**) Plot of lattice constant with respect to nanoparticle size obtained from the Williamson–Hall plot showing lattice expansion with decreasing particle size.

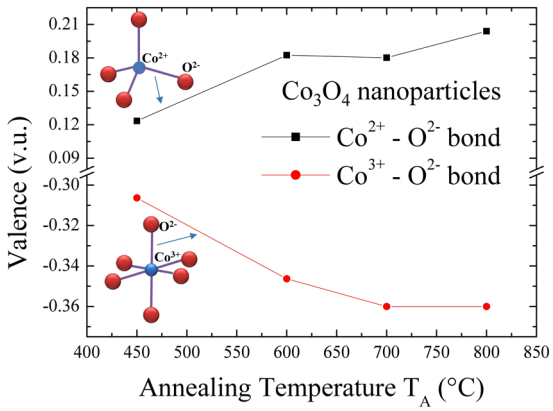

Figure 5. Plot of annealing temperatures dependence of the net valence of $Co^{2+}(0$ and $Co^{3+}(0)$, respectively.

Co^{3+} governed by various external sources like magnetic field, high pressure, temperature etc., have led to phenomena like diffusive charge transfer, a very large redshift of phonon-phonon interaction in the inverse spinel structure, as will be discussed in the Raman and magnetization analysis session.

Phonon Excitation in Co_3O_4 nanoparticles. Confocal Raman spectroscopy was utilized to study the size dependence of related phonon coupling of the cobalt cation of Co_3O_4 nanoparticles due to their high spatial resolution and sensitivity for probing atomic vibration. Figure 6(a) displays the series of Raman spectra for annealing temperatures ranging from 450 °C to 800 °C (bottom to top). Five main phonon excitations were observed at $T_A = 450$ °C, as shown at the bottom of Fig. 6(a), which are in good agreement with the values predicted by the

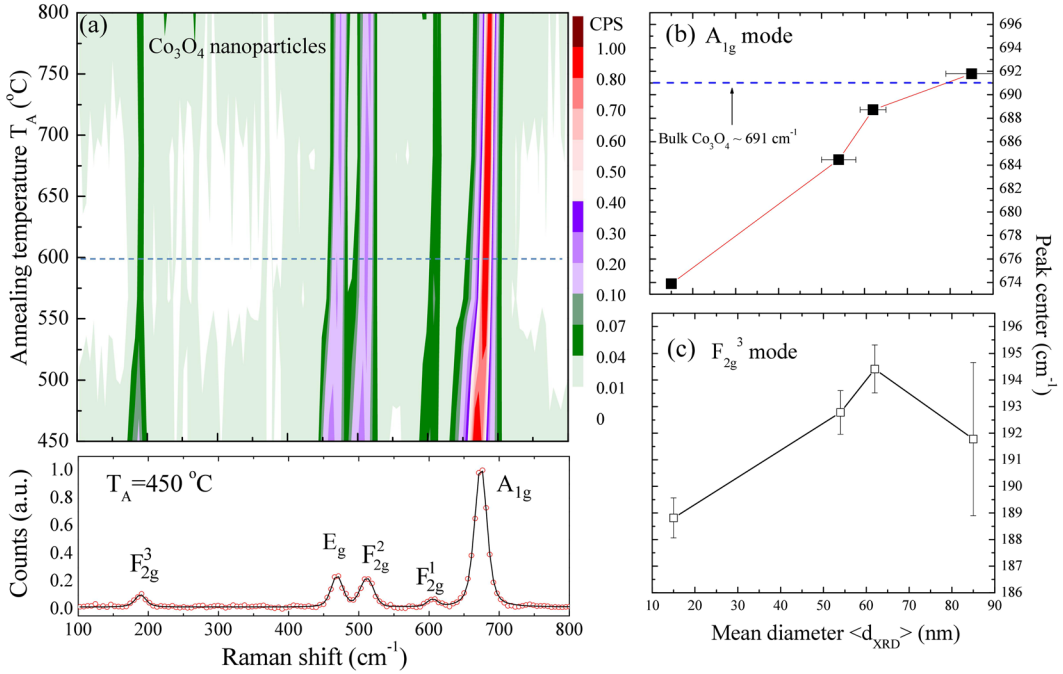

Figure 6. (**a**) Two-dimensional map of the intensity and T_A dependence of Raman patterns for Co_3O_4 NPs taken at room temperature. A selected Raman pattern taken at $T_A = 450$ °C is shown at the bottom, revealing a series of phonon modes excitations. Crystalline size dependency of (**b**) A_{1g} phonon peak center and (**c**) F^3_{2g} mode, respectively.

group theory and the related report of the Co_3O_4 nanoparticles[37,38], consisting of $F^3_{2g} + E_g + F^2_{2g} + F^1_{2g} + A_{1g}$[39–42]. The band at 674 cm^{-1} is viewed as the symmetric Co-O stretching vibration of the octahedral (CoO_6) group, which is assigned to the A_{1g} species in the O^7_h spectroscopic symmetry. The Raman bands with medium intensity located at 469 and 511.5 cm^{-1} have E_g and F^2_{2g} symmetry, respectively, whereas the weak band located at 605 cm^{-1} has the F^1_{2g} symmetry. The band at 188.8 cm^{-1} is attributed to the characteristics of the tetrahedral sites (CoO_4), which are attributed to the F^3_{2g} symmetry. This result further confirms the formation of the Co_3O_4 nanocrystals. The growth temperature T_A dependence of the phonon peak positions and intensities obtained from two-dimensional Raman images of Co_3O_4 nanoparticles are shown at the top of Fig. 6(a), where different colors present the peak intensity of the Raman patterns. As we can see from Fig. 6(a) below T_A ~ 600 °C, a significant shoulder is observed on the higher frequency of A_{1g} mode near the lower T_A regime of the Co_3O_4 nanoparticles. The quantitative analysis of anomalous behavior was carried out by peak profile fitting using the Voigt distribution function covering the whole regime. The detailed T_A dependences of the peak position and full widths at half maximum (*fwhm*) are summarized in the supplementary information of Table S3. Figure 6(b)–(c) presents the evolution of the peak center of the two selected A_{1g} and F^3_{2g} modes related to the vibrations of the octahedral position occupied by the Co^{3+} cation and the tetrahedral position occupied by Co^{2+} cation for various T_A, respectively. As the particle size d_{XRD} is reduced, the peak center of the A_{1g} mode rapidly shifts to a lower wave number by about 17 cm^{-1} (in comparison with the bulk value of 691 cm^{-1}) while simultaneously the F^3_{2g} mode down shifts about 3 cm^{-1}, revealing the finite size effect. Peak shift and asymmetrical broadening of the Raman line shape may lead to the important information related to the present Co_3O_4 nanoparticles under investigation. Tensile stress causes the Raman band to red shift. Lattice disorder and low dimensional crystals lead to the asymmetrical broadening and the downshifting of the A_{1g} mode. But another factor that results in an asymmetrical broadening and a shoulder on the higher frequency is the thermal heating process, which results in an increase of the lattice parameter near the lower T_A regime of Co_3O_4 nanoparticles, as can be found in the supplementary information of Table S1. This observation cannot be explained in terms of a change in stoichiometry with the decrease of particle size. Thus, the observed Raman shift and line-broadening is attributed to a size-dependent effect on the nanoparticles which is in good agreement with the previous reports[43].

Isothermal Magnetization Measurement. Isothermal magnetization hysteresis loop $M(H_a)$ measurement of Co_3O_4 nanoparticles was taken at temperatures 2 K and 300 K over a magnetic field of ± 10 kOe, as shown in Fig. 7. A coercivity $H_C = 19$ Oe is observed for 15 ± 1 nm NPs at 2 K (shown in 1st quadrant of the figure), thus exhibiting weak FM behavior of Co_3O_4 NPs and paramagnetic (PM) behavior at room temperature (shown in 4th quadrant figure). For bulk AFM material, below Néel temperature T_N, magnetization is expected to vary linearly with an applied field with zero coercivity (H_C) and remanence (M_r)[19]. The observed zero value of H_C, M_r and non-saturating behavior of $M(H_a)$ loop from Co_3O_4 nanoparticles measured at 2 K (below T_N) indicates the pure AFM behavior. Magnetic moments in Co_3O_4 arise solely because of spins of Co^{2+} ions having a small contribution from spin-orbit coupling[17]. On the other hand, the Co^{3+} ions at the octahedral sites are

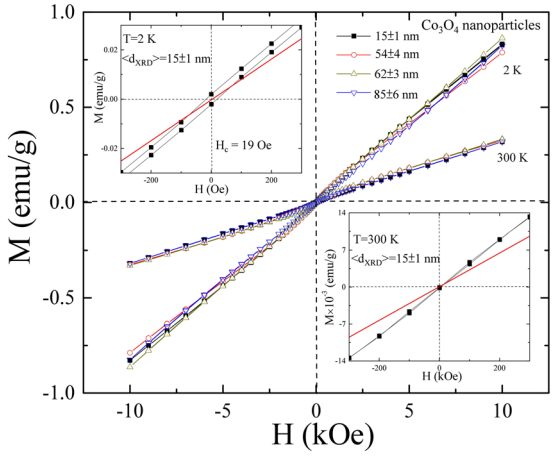

Figure 7. Isothermal hysteresis M(H) loop measured at 2 and 300 K for all Co_3O_4 NPs. In the inset of figure is the zero-field region M(H) loop for 15 ± 1 nm NPs measured at 2 K (1st quadrant) and 300 K (4th quadrant).

diamagnetic as a consequence of the splitting of *3d* levels by the octahedral crystal field and complete filling of t_{2g} levels due to which vacancies at the octahedral sites do not contribute to net magnetization. The observed linear increasing behavior of $M(H_a)$ loop above and below T_N is in good agreement with the previously reported mesoporous Co_3O_4 nanostructures[42]. However, in general, AFM metal oxide nanoparticles exhibit spin-glass and/or weak-ferromagnetic (FM) like behavior arising from the uncompensated surface spins[27,44,45]. The randomly oriented, uncompensated surface spins form the short-range ordered clusters of the spins which behave like weak-FM. Recently, Valan *et al.*[26] reported the observation of soft and weak-FM behavior from 45 and 29 nm Co_3O_4 nanoparticles synthesized by using microwave combustion method, which was ascribed to uncompensated surface spins and/or finite size effect. From the magnetic point of view, such nanoparticles behave like a core-shell having an uncompensated AFM core and a short-range ordered weak-FM shell. The intercoupling between the spins of AFM and FM at the interface results in the formation of a unidirectional anisotropy energy barrier, which gives rise to a hysteresis loop shift called an exchange bias phenomenon. The exchange bias phenomenon could be conventional (CEB)[46] or spontaneous exchange bias (SEB)[47]. Zeng *et al.*[35] reported the observation of a CEB field of −600 Oe from 25 nm Co_3O_4 nanoparticles using a cooling field of 50 kOe arising from the intercoupling between a spin-glass-like shell and an uncompensated AFM core. Wang *et al.*[42] also reported the observation of a CEB field of −530 Oe at 5 K from nanoporous Co_3O_4 rods (~30 nm nanocrystals) using a cooling field of 10 kOe arising from the intercoupling between the nanocrystals within the nanorods. During the last decades, several reports on Co_3O_4 nanoparticles have claimed the observation of the CEB effect with a maximum loop shift of −800 Oe using a cooling field of 70 kOe[19,48–51]. Similarly, a CEB effect due to the intercoupling between spins of the spin-glass-like or weak-FM shell and uncompensated AFM core has also been reported from nanoparticles of various AFM metal oxides such as NiO[52], CoO[53], MnO[54], Cr_2O_3[55] etc. However, the observation of such a high exchange bias field seems to be overestimated, which could be due to the pre-magnetization of surface spins in an external cooling field. Since, the value of CEB is dependent on several factors such as interfacial roughness, the complex spin structure, uncompensated spins at the interface, and particularly thickness that is on the long-range ordering of FM and AFM components as observed from several core-shell FM/AFM nanoparticles. In the last few years, the SEB effect has been observed in various systems from bulk, FM/AFM core/shell, and nanocomposite to a pure AFM nanostructure[56]. In our previous magnetic study of a NiO nanoparticles system[57], we also observed that the SEB field decreases with the increase of particle size. Therefore, for a proper understanding of the hysteresis loop shift in Co_3O_4 nanoparticles, a comprehensive magnetic study is needed. Furthermore, above the Néel temperature, the thermal energy overcomes the AFM ordering, and the material behaves paramagnetically. The $M(H_a)$ loop measured at 300 K shows paramagnetic like behavior with a zero value of H_C, M_r with linear increasing and non-saturating behavior of the magnetization with an applied magnetic field.

Temperature dependence of the magnetization measurement. The magnetic susceptibility of bulk AFM material increases with a measuring temperature below the T_N while above, it exhibits paramagnetic behavior[19]. To determine the temperature dependence of the magnetic moment of Co_3O_4 nanoparticles, two types of measurement were carried out, namely, using zero-field-cooled (ZFC) and field-cooled (FC) measurements with a rate of 2 K/min. For the ZFC measurement, the sample was initially cooled down from 300 K down to 2 K in a zero magnetic field, and the magnetization was recorded while warming the system in a magnetic field of 100 Oe. For the FC measurement, the sample was again cooled down from 300 K down to 2 K, but in a magnetic field of 100 Oe, magnetization was recorded while warming the system in the same applied magnetic field. Figure 8(a)–(d) shows the temperature dependency of magnetization M(T) with ZFC-FC modes for 15 ± 1, 54 ± 4, 62 ± 3, 85 ± 6 nm Co_3O_4 NPs in an applied field of 100 Oe. A high irreversible temperature (T_{irr}) defined by the temperature at which the FC curve starts to split from the ZFC curve, above 200 K is observed for 15 ± 1, 62 ± 3 and 85 ± 6 nm NPs, whereas 54 ± 4 nm NPs show T_{irr} ~ 60 K, relating to spin-glass-like behavior. Furthermore, from the M(T) curve for 15 ± 3 nm sample, two common characteristic features can be drawn. First, a blocking temperature T_B is defined as the maximum value of ZFC curve, which increases from 31 ± 1 to 38 ± 1 K as the particle

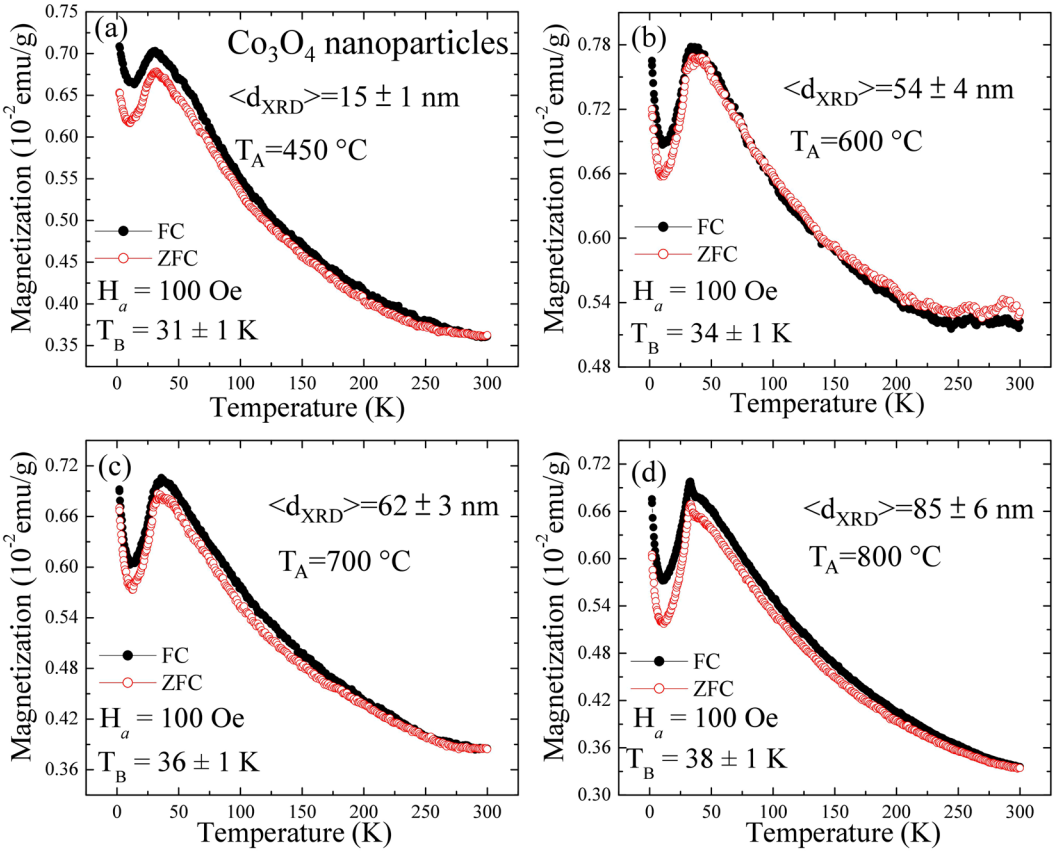

Figure 8. (**a**)–(**d**) Temperature dependent magnetization M(*T*) measured by using ZFC-FC process with 100 Oe applied field for 15 ± 1, 54 ± 4, 62 ± 3 and 85 ± 6 nm Co_3O_4 NPs.

size increases from 15 ± 1 to 85 ± 6 nm. Second, there is a sharp increasing behavior of magnetization at low temperature, defined as freezing temperature T_f = 11 K, as shown in Fig. 8(a). Similar temperature dependent magnetization behavior has been reported in several experimental ZFC-FC curves from Co_3O_4 nanoparticles[58,59]. However, there are also reports in which anomalous magnetic properties such as weak-ferromagnetism and SPM behavior have been reported from Co_3O_4 nanoparticles[60]. According to the Néel-Brown model[61,62], the uniaxial and non-interacting superparamagnetic nanoparticles exhibit a distribution of the anisotropy energy barrier due to polydispersity. If each particle gets blocked at the blocking temperature, T_B then in poly-dispersed nanoparticles, $T_B \approx KV/25k_B$ will be associated with the mean value of T_B, where K is the effective anisotropy energy density, V is particle volume and k_B is Boltzmann's constant. The effective anisotropy comprises several intrinsic factors such as volume, surface, shape, exchange and magnetocrystalline anisotropies. According to the above expression, the value of T_B increases with particle size, which is in good agreement with the observed increasing behavior of T_B = 34 ± 1, 36 ± 1 and 38 ± 1 K from Co_3O_4 nanoparticles of sizes 54 ± 4, 62 ± 3 and 85 ± 6 nm, respectively. The calculated value of K, summarized in the supplementary information of Table S4, decreases from 5331 J/m^3 to 80 J/m^3 with the increase of particle size from 15 ± 1 nm to 85 ± 6 nm, respectively. The K is much smaller than reported value of 90 kJ/m^3 from the 3 nm sized Co_3O_4 nanoparticles (T_B = 3 K)[63]. It shows the opposite behavior compared to the blocking temperature due to a reduction of particle mean volumes at lower sizes. This anomalous enhancement of the effective anisotropy indicates that the maximum in the ZFC magnetization does not correspond to the typical blocking temperature of the non-interacting particles, where inter particle interaction, including dipole-dipole and exchange interaction from weak-ferromagnetic shell moment of Co_3O_4 nanoparticles, plays a significant role in the temperature dependence of the magnetization. The irreversible temperature, T_{irr} determines the highest value for T_B in the system, whereas T_f at lower temperature corresponds to the surface spin freezing temperature. The temperature $T_f \sim 10$ K is associated with the freezing of uncompensated surface spins which has been reported a number of times from different size Co_3O_4 nanoparticles.

Finite size effect on the Néel temperature with Co_3O_4 nanoparticles. In magnetic nanomaterials, by reducing the particle size, an intrinsic finite size effect causing a reduction in the magnetic ordering temperature occurs. The Co^{3+} ions at the octahedral sites are diamagnetic while the spin moments of the Co^{2+} ions at the tetrahedral sites exhibit AFM ordering at $T < T_N = 40$ K[17]. In the nanoscale region, some experiments have reported a reduced T_N. For example, $T_N \sim 30$ K has been observed with 8 nm Co_3O_4 nanoparticles and 15 ± 2 K with 4.3 nm nanoparticles[18–20]. Experimentally, the value of Néel temperature T_N can be obtained as the peak in

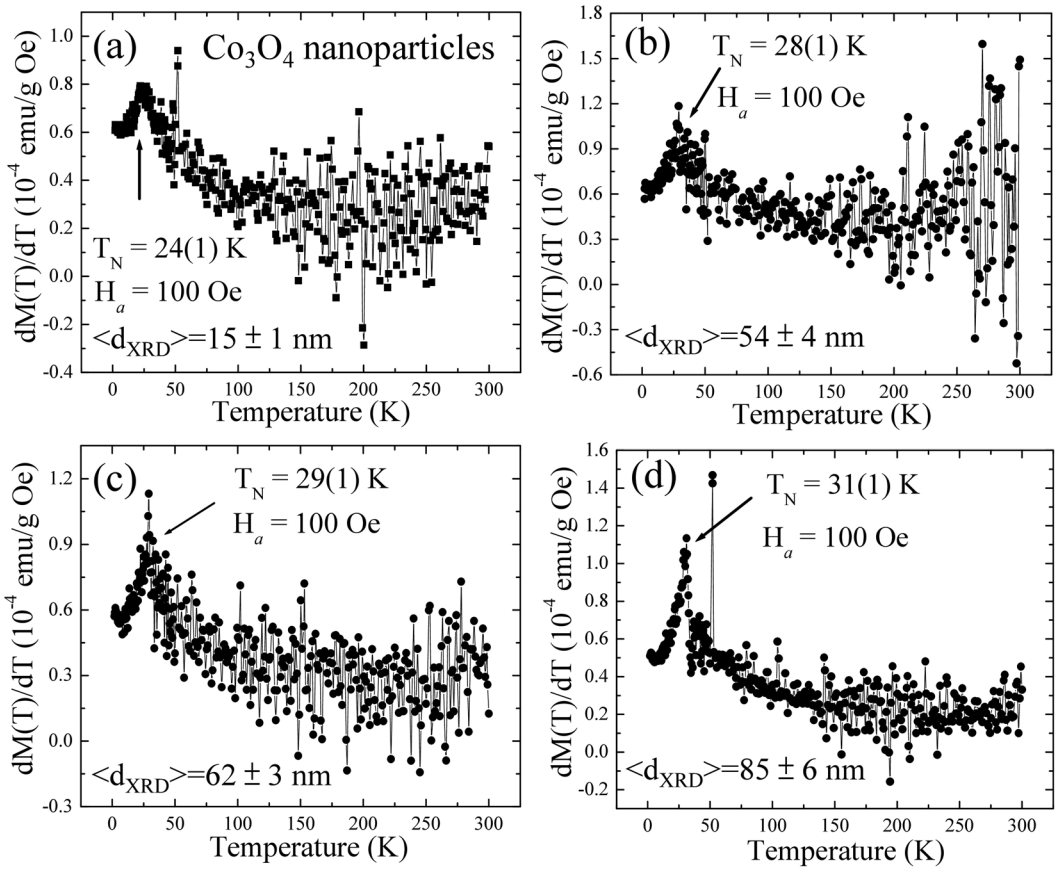

Figure 9. (**a**)–(**d**) Temperature dependence of differential magnetization $\partial M(T)/\partial T$ for 15 ± 1, 54 ± 4, 62 ± 3 and 85 ± 6 nm Co_3O_4 NPs.

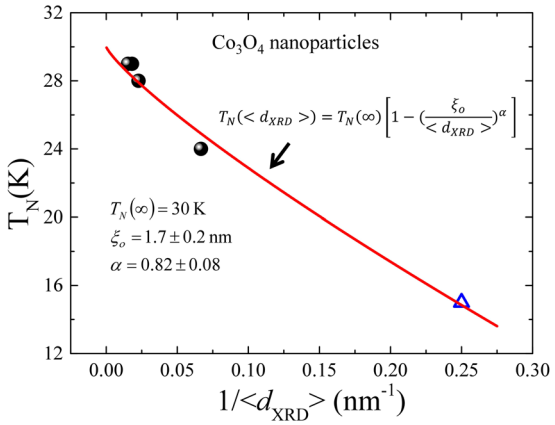

Figure 10. Plot of Néel transition temperature T_N verses inverse of particles size of Co_3O_4 NPs, where the solid line is fit by using the finite size scaling relation. The open triangle are the data points taken from reference number 6.

the $\partial M(T)/\partial T$ versus T plot[64], as shown in Fig. 9(a)–(d). These plots yield $T_N = 24 \pm 1$, 28 ± 1, 29 ± 1 and 31 ± 1 K from Co_3O_4 nanoparticles of size 15 ± 1, 54 ± 4, 65 ± 3 and 85 ± 6 nm, respectively. The value of T_N for 65 ± 3 and 85 ± 6 nm is close to the reported value of 30 K for bulk Co_3O_4[18,19], which is in good agreement with structural and atomic percent results as observed from SR-XRD and EDS measurements. The decrease of $T_N = 24 \pm 1$ K for 15 ± 1 nm Co_3O_4 nanoparticles can be understood by considering the intrinsic finite size effect on the correlation length of the magnetic ordering temperature, which has been reported from FM, AFM[53,58] and ferromagnetic[65] nanostructured materials. Figure 10 displays the inverse of particles size dependency of T_N, where the solid line is fitted to the finite size scaling relation defined as: $T_N(<d_{XRD}>) = T_N(\infty)\left[1 - \left(\frac{\xi_0}{<d_{XRD}>}\right)^{\alpha}\right]$, where $T_N(\infty) = 30$ K

for bulk Co_3O_4, ξ_o is the correlation length of bulk phase at zero temperature and α the shift exponent. Fitting yields $\alpha = 0.82 \pm 0.08$ and $\xi_o = 1.7 \pm 0.2\,nm$. The value of α is close to the theoretical predicted value of 1 by mean field theory[66], but lower than the 3D Heisenberg model[67] (1.4) and Ising Hamiltonian[68] (1.6) values. The correlation length ξ_o is about ~2 times the lattice constant of Co_3O_4, which is agreed with the predicted value of 1.6 nm, derived from Monte Carlo simulation[69].

Discussion

The crystalline, optical and magnetic properties of microwave assisted synthesized Co_3O_4 NPs (15 to 85 nm) have been systematically investigated. The observed non-stoichiometry nature from EDS spectra and expansion in (Co^{2+}-O^{2-}) bond length from SR-XRD confirm that weak magnetism from 15 ± 1 nm NPs (at 2 K) is associated with the cobalt vacancies Co^{2+} at the tetrahedral site. Nanoscale size effects lead to lattice expansion, line-broadening, red shift in the phonon wave number and reduction in the Néel temperature T_N of Co_3O_4 NPs, giving a short-range magnetic correlation length $\xi_o \sim 1.7$ nm from the fitting of the finite size scaling model. The size dependency of T_N and the observed line-broadening and red shift in the phonon wave number show the effect of the finite size effect[10]. However, it remains questionable, why only 15 ± 1 nm Co_3O_4 NPs shows a hysteresis loop below the Neel transition temperature. In general, based on the experimental conditions, the dynamically post-annealing of microwave assisted grown nanocrystals could involve many competing atomic movements, including the transport of atomic-size matter from core to surface and on-surface reconstruction. In this study, the annealing time is fixed, thus T_A is the only factor to affect the size and points of defects (cobalt vacancies) in the nanocrystals. By taking into account the observed experimental results from SR-XRD and the EDS spectra, we propose that cobalt vacancies in Co_3O_4 NPs are located at the tetrahedral Co^{2+} site. These vacancies in the 15 nm sample are mostly distributed on the surface since the surface-to-volume ratio is high, thus weak magnetism comes from defect interactions. The above finding also opens an avenue for further increase of intrinsic FM properties by controlling the density of defects under experimental conditions. Moreover, the mechanism of the AFM transition of the Co-3*d* electrons in Co_3O_4 is discussed, and we show that the occurrence of finite size effect on the magnetic ordering. The reduction of T_N with the decrease of particles size is attributed to the intrinsic finite size effect. These results open a new route to achieve and manipulate short-range magnetic states in spintronic devices.

Method

Cobalt (II) nitrate hexahydrate ($Co(NO_3)_2{\cdot}6H_2O$, 99.99%), Poly Ethyl Glycol [PEG] and ammonia solution (30%) [NH_4OH] were the only chemicals used during the synthesis. All the chemicals were purchased from Sigma-Aldrich and used as received. Deionized water (DIW) is used as a solvent. Co_3O_4 NPs were synthesized using the microwave irradiation technique. Cobalt nitrate hexahydrate and ammonia solution were used as precursors and distilled water as a solvent. Initially, a 0.4 M aqueous solution of cobalt nitrate under continuous stirring was prepared at room temperature. Ammonia solution was added drop by drop until the pH of the solution became 10. The solution turns into a dark green slurry, suggesting the formation of a stable cobalt ammonia complex. For the stabilization of Co_3O4 nanoparticles, 0.5 g of PEG was dissolved in 10 mL of distilled water in 100 mL of beaker; then 3 mL of PEG solution was added to the slurry. This mixture was exposed to microwave irradiation at 80 °C for 15 minutes at 140 watt power under constant stirring. Due to microwave heating, the cobalt ammonia complex decomposes forming a dark green precipitate. This precipitate was separated from the supernatant liquid by centrifuging at 2000 rpm for 2 minutes. The residue was washed with distilled water and then with ethanol 2-3 times. The dark green color residue was then dried overnight in air. And the obtained resultant sample, namely as-grown Co_3O_4 sample, was divided into four sets and annealed using a high-temperature horizontal quartz tube furnace. The complete post-synthesis process is as follows:(1) The as-grown sample was put on a porcelain boat and placed in a quartz tube in the middle region of a heated oven. (2) The pressure of the quartz tube was reduced to less than 1×10^{-2} Torr by a mechanical pump. (3) The heating temperature in a quartz tube was set for various as-grown samples in a temperature range of $T_A = 450$–800 °C, respectively. (4) After the temperature was stabilized, a mixed gas of oxygen (20 *sccm*) and argon (80 *sccm*) was introduced into the tube, and the pressure was kept at 760 Torr by a flux controller. (5) The boat was heated at a set temperature for two hours with a heating rate of 5 K/min and cooled down to room temperature naturally after the heating. (6) Finally, these resultant samples were saved in a low-pressure container to avoid further oxidation. Field-emission scanning electron microscopy (FE-SEM, JEOL JSM-6500F) microscope and energy dispersive spectroscopy (EDS; Inca x-sight model 7557, Oxford Instruments, Abingdon, Oxfordshire, U.K.) were utilized to investigate the morphology, size distribution of nanoparticles, and the atomic percentages of cobalt and oxygen. Detailed crystal structure measurement was carried out through a synchrotron radiation x-ray diffraction (SR-XRD) with a BL01C2 beam line and an incident wavelength of $\lambda = 0.7749$ Å at the National Synchrotron Radiation Research Center in Taiwan (for more detail see the ref.[21]). Confocal Raman spectrometer (α−300, WiTec Pte. Ltd., Ulm, Germany) with a 488-nm Ar ion laser (CVI Melles Griot, Carlsbad, CA)was used to measure the multi-phonon properties of Co_3O_4 nanoparticles.

Note: SRG and ACG share equal weightage in this manuscript. ACG is currently affiliated to the Center for Condensed Matter Sciences, National Taiwan University, Taipei, Taiwan.

References

1. Li, W. Y., Xu, L. N. & Chen, J. Co_3O_4 Nanomaterials in Lithium-Ion Batteries and Gas Sensors. *Adv. Funct. Mater.* **15**, 851–857 (2005).
2. Wang, R. M. *et al*. Porous nanotubes of Co_3O_4: Synthesis, characterization, and magnetic properties. *Appl. Phys. Lett.* **85**, 2080–2082 (2004).

3. Wang, X. *et al*. High gas-sensor and supercapacitor performance of porous Co_3O_4 ultrathin nanosheets. *RSC Adv.* **5**, 17938–17944 (2015).
4. Maruyama, T. & Arai, S. Electrochromic Properties of Cobalt Oxide Thin Films Prepared by Chemical Vapor Deposition. *J. Electrochem. Soc.* **143**, 1383–1386 (1996).
5. Mate, V. R., Shirai, M. & Rode, C. V. Heterogeneous Co_3O_4 catalyst for selective oxidation of aqueous veratryl alcohol using molecular oxygen. *Catal. Commun.* **33**, 66–69 (2013).
6. Chou, S.-L., Wang, J.-Z., Liu, H.-K. & Dou, S.-X. Electrochemical deposition of porous Co_3O_4 nanostructured thin film for lithium-ion battery. *J. Power Sources* **182**, 359–364 (2008).
7. Casas-Cabanas, M. *et al*. Defect Chemistry and Catalytic Activity of Nanosized Co_3O_4. *Chem. Mater.* **21**, 1939–1947 (2009).
8. Xie, X., Li, Y., Liu, Z.-Q., Haruta, M. & Shen, W. Low-temperature oxidation of CO catalysed by Co_3O_4 nanorods. *Nature* **458**, 746–749 (2009).
9. Shin, C. *et al*. Structural characterization and electrochemical properties of Co_3O_4 anode materials synthesized by a hydrothermal method. *Nanoscale Res. Lett.* **7**, 73 (2012).
10. George, G. & Anandhan, S. Structural characterization of nano-crystalline Co_3O_4 ultra-fine fibers obtained by sol–gel electrospinning. *J. Sol-Gel Sci. Technol.* **67**, 256–266 (2013).
11. Farhadi, S., Pourzare, K. & Bazgir, S. Co_3O_4 nanoplates: Synthesis, characterization and study of optical and magnetic properties. *J. Alloys Compd.* **587**, 632–637 (2014).
12. Anandha Babu, G., Ravi, G., Hayakawa, Y. & Kumaresavanji, M. Synthesis and calcinations effects on size analysis of Co_3O_4 nanospheres and their superparamagnetic behaviors. *J. Magn. Magn. Mater.* **375**, 184–193 (2015).
13. Furlanetto, G. & Formaro, L. Precipitation of Spherical Co_3O_4 Particles. *J. Colloid Interface Sci.* **170**, 169–175 (1995).
14. Cao, L., Lu, M. & Li, H.-L. Preparation of Mesoporous Nanocrystalline Co_3O_4 and Its Applicability of Porosity to the Formation of Electrochemical Capacitance. *J. Electrochem. Soc.* **152**, A871–A875 (2005).
15. Wang, L., Deng, J., Lou, Z. & Zhang, T. Nanoparticles-assembled Co_3O_4 nanorods *p*-type nanomaterials: One-pot synthesis and toluene-sensing properties. *Sens. Actuators B: Chem.* **201**, 1–6 (2014).
16. Angelov, S., Zhecheva, E., Stoyanova, R. & Atanasov, M. Bulk defects in Co_3O_4, pure and slightly doped with lithium, revealed by EPR of the tetrahedral Co^{2+} ions. *J. Phys. Chem. Solids* **51**, 1157–1161 (1990).
17. Roth, W. L. The magnetic structure of Co_3O_4. *J. Phys. Chem. Solids* **25**, 1–10 (1964).
18. Khriplovich, L. M., Kholopov, E. V. & Paukov, I. E. Heat capacity and thermodynamic properties of Co_3O_4 from 5 to 307 K Low-temperature transition. *J. Chem. Thermodyn.* **14**, 207–217 (1982).
19. Dutta, P., Seehra, M. S., Thota, S. & Kumar, J. A comparative study of the magnetic properties of bulk and nanocrystalline Co_3O_4. *J. Phys. Condens. Matter* **20**, 015218 (2008).
20. Resnick, D. A. *et al*. Magnetic properties of Co_3O_4 nanoparticles mineralized in Listeria innocua Dps. *J. Appl. Phys.* **99**, 08Q501 (2006).
21. Gandhi, A. C. *et al*. Short-Range Magnon Excitation in NiO Nanoparticles. *J. Phys. Chem. C* **117**, 18666–18674 (2013).
22. Gaikwad, S. S. *et al*. Oxygen induced strained ZnO nanoparticles: an investigation of Raman scattering and visible photoluminescence. *J. Mater. Chem. C* **2**, 7264–7274 (2014).
23. Gandhi, A. *et al*. Growth mechanism and magnon excitation in NiO nanowalls. *Nanoscale Res. Lett.* **6**, 1–14 (2011).
24. Gandhi, A. C. *et al*. *In Situ* Confocal Raman Mapping Study of a Single Ti-Assisted ZnO Nanowire. *Nanoscale Res. Lett.* **5**, 581–586 (2010).
25. Lin, P.-Y., Gandhi, A. C. & Wu, S. Y. Size effect of strong-coupled superconducting In_2Bi nanoparticles: An investigation of short-range electron phonon coupling. *J. Appl. Phys.* **117**, 17E316 (2015).
26. Valan, M. F., Manikandan, A. & Antony, S. A. A Novel Synthesis and Characterization Studies ofMagnetic Co_3O_4 Nanoparticles. *J. Nanosci. Nanotechnol.* **15**, 4580–4586 (2015).
27. Farhadi, S., Safabakhsh, J. & Zaringhadam, P. Synthesis, characterization, and investigation of optical and magnetic properties of cobalt oxide (Co_3O_4) nanoparticles. *J. Nanostruct. Chem.* **3**, 69 (2013).
28. Wu, S. Y., Ji, J.-Y., Chou, M.-H., Li, W.-H. & Chi, G. C. Low-temperature phase separation in GaN nanowires: An *in situ* x-ray investigation. *Appl. Phys. Lett.* **92**, 161901 (2008).
29. Prabhu, Y., Rao, K., Kumar, V. & Kumari, B. X-Ray Analysis by Williamson-Hall and Size-Strain Plot Methods of ZnO Nanoparticles with Fuel Variation. *World Journal of Nano Science and Engineering* **4**, 8 (2014).
30. Patterson, A. L. The Scherrer Formula for X-Ray Particle Size Determination. *Phys. Rev.* **56**, 978–982 (1939).
31. Rao, K. V. & Sunandana, C. S. Co_3O_4 nanoparticles by chemical combustion: Effect of fuel to oxidizer ratio on structure, microstructure and EPR. *Solid State Commun.* **148**, 32–37 (2008).
32. Ichiyanagi, Y. & Yamada, S. The size-dependent magnetic properties of Co_3O_4 nanoparticles. *Polyhedron* **24**, 2813–2816 (2005).
33. Makhlouf, M. T., Abu-Zied, B. M. & Mansoure, T. H. Direct Fabrication of Cobalt Oxide Nanoparticles Employing Sucrose as a CombustionFuel. *J. Nanopart.* **2013**, 384350 (2013).
34. Lv, L., Su, Y., Liu, X., Zheng, H. & Wang, X. Synthesis of cellular-like Co_3O_4 nanocrystals with controlled structural, electronic and catalytic properties. *J. Alloys Compd.* **553**, 163–166 (2013).
35. Zeng, R., Wang, J. Q., Chen, Z. X., Li, W. X. & Dou, S. X. The effects of size and orientation on magnetic properties and exchange bias in Co_3O_4 mesoporous nanowires. *J. Appl. Phys.* **109**, 07B520 (2011).
36. O'Keefe, M. & Hyde, B. G. Some structures topologically related to cubic perovskite ($E2_1$), ReO_3 ($D0_9$) and Cu_3Au ($L1_2$). *Acta Crystallogr.* **B33**, 3802 (1997).
37. Jiang, J. & Li, L. Synthesis of sphere-like Co_3O_4 nanocrystals via a simple polyol route. *Mater. Lett.* **61**, 4894–4896 (2007).
38. Lorite, I., Romero, J. J. & Fernandez, J. F. Infulence of the nanoparticles agglomeration state in the quantum-confinement effects: Experimental evidences. *AIP Adv.* **5**, 037105 (2015).
39. Hadjiev, V. G., Iliev, M. N. & Vergilov, I. V. The Raman spectra of Co_3O_4. *J. Phys. C. Solide State Phys.* **21**, L199 (1988).
40. Rashad, M., Rüsing, M., Berth, G., Lischka, K. & Pawlis, A. CuO and Co_3O_4 Nanoparticles: Synthesis, Characterizations, and Raman Spectroscopy. *J. Nanomater.* **2013**, 714853 (2013).
41. Lorite, I., Romero, J. J. & Fernández, J. F. Effects of the agglomeration state on the Raman properties of Co_3O_4 nanoparticles. *J. Raman Spectrosc.* **43**, 1443–1448 (2012).
42. Wang, G. *et al*. Hydrothermal Synthesis and Optical, Magnetic, and Supercapacitance Properties of Nanoporous Cobalt Oxide Nanorods. *J. Phys. Chem. C* **113**, 4357–4361 (2009).
43. Gouadec, G. & Colomban, P. Raman Spectroscopy of nanomaterials: How spectra relate to disorder, particle size and mechanical properties. *Prog. Cryst. Growth Ch. Mater.* **53**, 1–56 (2007).
44. Jin, H. *et al*. Fabrication of Mesoporous Co_3O_4 from LP-FDU-12 via Nanocasting Route and Effect of Wall/Pore Size on Their Magnetic Properties. *J. Phys. Chem. C* **116**, 13374–13381 (2012).
45. Ichiyanagi, Y., Kimishima, Y. & Yamada, S. Magnetic study on Co_3O_4 nanoparticles. *J. Magn. Magn. Mater.* **272–276**, E1245–E1246 (2004).
46. Nogués, J. *et al*. Exchange bias in nanostructures. *Phys. Rep.* **422**, 65–117 (2005).
47. Saha, J. & Victora, R. H. Spontaneous exchange bias: Unidirectional anisotropy in an otherwise isotropic system. *Phys. Rev. B* **76**, 100405 (2007).

48. Zhu, H. T. *et al*. Synthesis and magnetic properties of antiferromagnetic Co_3O_4 nanoparticles. *Physica B: Condens. Matter.* **403**, 3141–3145 (2008).
49. Makhlouf, S. A. Magnetic properties of Co_3O_4 nanoparticles. *J. Magn. Magn. Mater.* **246**, 184–190 (2001).
50. Lv, P., Zhang, Y., Xu, R., Nie, J.-C. & He, L. Anomalous magnetic properties of 7 nm single-crystal Co_3O_4 nanowires. *J. Appl. Phys.* **111**, 013910 (2012).
51. Salabaş, E. L., Rumplecker, A., Kleitz, F., Radu, F. & Schüth, F. Exchange Anisotropy in Nanocasted Co_3O_4 Nanowires. *Nano Lett.* **6**, 2977–2981 (2006).
52. Yang, Z. *et al*. A series of unexpected ferromagnetic behaviors based on the surface-vacancy state: an insight into NiO nanoparticles with a core-shell structure. *RSC Adv.* **4**, 46133–46140 (2014).
53. He, X. *et al*. Transition Temperature of Wurtzite CoO Nanocrystals as Revealed in Comprehensive Magnetic Characterization. *J. Phys. Chem. C* **118**, 13898–13903 (2014).
54. Luo, Y. *et al*. Exchange bias effect in single crystalline phase MnO nanoparticles. *Acta Phys. Sin* **62**, 176102 (2013).
55. Makhlouf, S. A. Magnetic properties of Cr_2O_3 *Nanoparticles. J. Magn. Magn. Mater.* **272–276**, 1530–1532 (2004).
56. Maity, T., Goswami, S., Bhattacharya, D. & Roy, S. Superspin Glass Mediated Giant Spontaneous Exchange Bias in a Nanocompositeof $BiFeO_3$-$Bi_2Fe_4O_9$. *Phys. Rev. Lett.* **110**, 107201 (2013).
57. Gandhi, A. C., Pant, J. & Wu, S. Y. Dense inter-particle interaction mediated spontaneous exchange bias in NiO nanoparticles. *RSC Adv.* **6**, 2079–2086 (2016).
58. He, L., Chen, C., Wang, N., Zhou, W. & Guo, L. Finite size effect on Néel temperature with Co_3O_4 nanoparticles. *J. Appl. Phys.* **102**, 103911 (2007).
59. Bisht, V. & Rajeev, K. P. Unusual superparamagnetic behavior of Co_3O_4 nanoparticles. *arXiv* **1008**, 5245 (2010).
60. Dong, Z., Fu, Y., Han, Q., Xu, Y. & Zhang, H. Synthesis and Physical Properties of Co_3O_4 Nanowires. *J. Phys. Chem. C* **111**, 18475–18478 (2007).
61. Néel, L. Théorie du traînage magnétique des ferromagnétiques en grains fins avec application aux terres 5 cuites. *Ann Geophys (CNRS)* **5**, 37 (1949).
62. Brown, W. Thermal Fluctuations of a Single-DomainParticle. *Phys. Rev.* **130**, 1677–1686 (1963).
63. Takada, S. *et al*. Intraparticle Magnetic Properties of Co_3O_4 Nanocrystals. *Nano Lett.* **1**, 379–382 (2001).
64. Fisher, M. E. Relation between the specific heat and susceptibility of an antiferromagnet. *Philosophical Magazine* **7**, 1731–1743 (1962).
65. Tang, Z. X., Sorensen, C. M., Klabunde, K. J. & Hadjipanayis, G. C. Size-dependent Curie temperature in nanoscale $MnFe_2O_4$particles. *Phys. Rev. Lett.* **67**, 3602–3605 (1991).
66. Fisher, M. E. & Barber, M. N. Scaling Theory for Finite-Size Effects in the Critical Region. *Phys. Rev. Lett.* **28**, 1516–1519 (1972).
67. Chen, K., Ferrenberg, A. M. & Landau, D. P. Static critical behavior of three-dimensional classical Heisenberg models: A high-resolution Monte Carlo study. *Phys. Rev. B* **48**, 3249–3256 (1993).
68. Ferrenberg, A. M. & Landau, D. P. Critical behavior of the three-dimensional Ising model: A high-resolution Monte Carlo study. *Phys. Rev. B* **44**, 5081–5091 (1991).
69. Iglesias, Ò. & Labarta, A. Finite-size and surface effects in maghemite nanoparticles: Monte Carlo simulations. *Phys. Rev. B* **63**, 184416 (2001).

Acknowledgements

This work was supported by the Ministry of Science and Technology (MOST) of the Republic of China under the projects MOST-106–2112-M-259–001(SYW) and MOST-105–2112-M-259–003 (SYW). We would also like to thank the Indian Space Research Organization and the University of Pune from the grant No. GOI-A-337(B) (111) (J.P.).

Author Contributions

A.C.G., S.S.G., and S.R.G. analyzed the data. J.P. and S.R.G. grew the sample. T.S.C., C.L.C., and Y.R.M. contributed the experimental facilities for the x-ray, confocal Raman, and FE-SEM measurements, respectively. A.C.G., J.P., and S.Y.W. wrote the paper, and all authors discussed the contents and approved the final version.

Additional Information

Supplementary information accompanies this paper at https://doi.org/10.1038/s41598-017-18563-9.

Competing Interests: The authors declare that they have no competing interests.

Publisher's note: Springer Nature remains neutral with regard to jurisdictional claims in published maps and institutional affiliations.